NANO LETTERS

Letter

pubs.acs.org/NanoLett

Label-Free Specific Detection of Femtomolar Cardiac Troponin Using an Integrated Nanoslit Array Fluidic Diode

Yifan Liu and Levent Yobas*

Department of Electronic and Computer Engineering, The Hong Kong University of Science and Technology, Clear Water Bay, Kowloon, Hong Kong S. A. R

Supporting Information

ABSTRACT: We demonstrate here for the first time the utility of an integrated nanofluidic diode for detecting and quantifying physiologically relevant macromolecules. Troponin T, a key human cardiac protein biomarker, was selectively and rapidly detected free of labels for concentrations down to 10 fg/mL (~0.3 fM) in buffer as well as 10 pg/mL (~300 fM) in untreated human serum. This ultrasensitive detection arises from monolithic integration of a unique nanofluidic diode structure that is highly robust and amenable to site-specific surface modification. The structure features a planar nanoslit array where each nanoslit is defined at a nominal width of 70 nm over a micrometer-scale silicon trench without the use of high-resolution patterning techniques. Through vapor deposition, a glass layer is placed at a nonuniform thickness, tapering the trench profile upward and contributing to the triangular nanoslit structure. This asymmetric profile is essential for ionic current rectification noted here at various pH values, ionic strengths, and captured target species, which modulate the surface-charge density within the sensitive region of the nanoslit. The nanoslit, unlike nanopores, offers only 1D confinement, which appears to be adequate for reasonable rectification. The measurements are found in quantitative agreement with the diode simulations for the first time based on a pH- and salt-dependent surface-charge model.

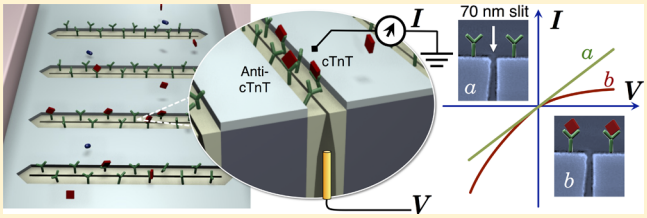

KEYWORDS: *Nanofluidic diode, biosensor, ionic current rectification, biomarker, troponin*

In recent years, increasing attention has been devoted to new methods of detecting and quantifying biomolecules because of their paramount importance to modern clinical and biological fields. Biomarker detection, for instance, is widely used for rapid diagnosis and prognosis of critical medical diseases and conditions such as cancer and myocardial infarction. The broad acceptability of biosensing techniques depends mostly on how well they perform the daunting task of rapidly identifying extremely rare analytes in complex biological samples. This demand, however, is barely met by conventional biosensing techniques such as enzyme-linked immunosorbent assay (ELISA),[1] microcantilevers,[2] and surface plasmon resonance (SPR).[3] Recent advances in nanometer-scaled field-effect biosensors such as nanowires,[4−7] nanotubes,[8−11] and nanobelts[12] have set a new record in terms of detection limits, speed, and portability. These revolutionary biosensors exhibit extremely high sensitivity for biomolecules like DNA[13] and proteins[14] and also show a capacity to detect the presence of single macromolecular complexes like viruses.[5] Nevertheless, certain practical issues must be addressed before these nanobiosensors can become ubiquitous, particularly issues related to their robustness, manufacturability, and cost effectiveness.[15]

The past decade has witnessed the burgeoning of nanofluidics and its extensive use in chemical and biomedical applications.[16] The unique ion-transport behavior that is exhibited in nanochannels has led to the development of numerous innovative devices such as nanofluidic diodes[17,18] and transistors.[19,20] Nanofluidic diodes refer to the nanoporous structures that allow ion flux in one direction while suppressing it in the reverse direction. This effect occurs in a nanochannel in which the critical dimension is comparable to the Debye length and the symmetry across the structure is broken as a result of an nonuniform channel profile,[21] an uneven surface charge,[22] or a lopsided buffer concentration.[23] The phenomenon is explained by the asymmetric electrostatic impact of the charged surface on the fluid confined within the nanochannel, which results in the accumulation and depletion of ions in response to oppositely biased polarities.[17] These active nanofluidic devices share certain key features with semiconducting nanosensors in that both function based on the field-effect principle and exhibit extremely large surface-to-volume ratios; both of these features are essential for ultrasensitive and rapid electrical biosensing.

Considerable effort has been devoted to the development of ionic-current diodes that can rapidly and sensitively detect biomolecules. Notable examples include the real-time detection of cancer-biomarker proteins by using antibody-functionalized nanopipettes[24] and the recognition of streptavidin through biotin-activated nanoporous membranes.[25] In these studies,

Received: August 24, 2014
Revised: October 29, 2014
Published: November 4, 2014

   dx.doi.org/10.1021/nl5032524 | *Nano Lett.* 2014, 14, 6983−6990

however, the detection limit barely went below the picomolar level.[24−28] This was mostly because of the loss of precious targets through specific or nonspecific surface adsorption that occurs outside the active regions; applying surface passivation or functionalization selectively to these irregular, and often delicate structures is technically challenging.[24] Thus, monolithic integration of such current-rectifying structures can greatly enhance their robustness and functionality and make them highly susceptible to selective surface modification. Integrated nanofluidic diodes have been demonstrated by the pioneering studies of several research groups. Karnik et al. demonstrated ionic transport rectification in a chip-based bipolar nanofluidic diode,[29] and Perry et al. fabricated in-plane asymmetric nanofunnels and studied their ionic current rectification.[30] However, these integrated nanofluidic diodes have yet to be explored for selective and quantitative detection of a specific biomolecule of interest. Moreover, the fabrication of these devices relies on advanced lithography[30] or specialized patterning techniques (e.g., diffusion-limited patterning),[29] which might limit their throughput, cost-effectiveness, and potential for widespread use.

In this Letter, we introduce a novel monolithically integrated nanofluidic diode and demonstrate for the very first time the use of a monolithically integrated nanofluidic diode for sensitive and label-free detection of physiologically relevant macromolecules. As schematically illustrated in Figure 1a, the device features a planar glass nanoslit array that displays a unique tapered profile. This asymmetric nanostructure is formed when a glass layer is nonconformally deposited in high aspect-ratio micrometer-scale trenches in silicon[31] and therefore its fabrication does not need high-resolution advanced lithography. The device rectifies ionic currents in response to the surface charge surrounding the asymmetric nanoslits, which, unlike nanopores[26] or nanopipettes,[21] feature 1D rather than 2D confinement. To the best of our knowledge, no such ionic current-rectifying structure has been reported to date.

To characterize the device presented herein, we investigated its ionic current-rectifying behavior under various buffer conditions (pH and ionic strength) and performed numerical simulations in order to shed light on the underlying physical process. The simulation results strongly agreed with the experimental data, further confirming that 1D nanoconfinement supports ionic current rectification. We then demonstrated that our device is capable of detecting a clinically relevant protein biomarker, human cardiac troponin T (cTnT). The serum cTnT level, together with that of human cardiac troponin I, is regarded as the most effective marker for acute myocardial infarction.[32,33] Following heart trauma, these molecules are released from damaged cardiac muscles into the bloodstream.

We selectively functionalized the nanoslit surface with antibodies specific to cTnT through a passivation layer patterned to mask the remaining planar regions (Figure 1a). The biosensing concept is illustrated at the level of a single nanoslit in Figure 1b. At this stage, an almost linear current−voltage (I−V) response is obtained because of the neutral antibody layer. However, once the negatively charged cTnT molecules are captured, they modulate the surface charge and thus enrich cations within the slit, which consequently leads to the current rectification. The process can be readily detected by directly monitoring the I−V response. Using this strategy, we were able to detect 10 fg/mL (~0.3 fM) cTnT in buffer and 10 pg/mL (~300 fM) cTnT in human serum with acceptable selectivity and detection speed. The performance of our device

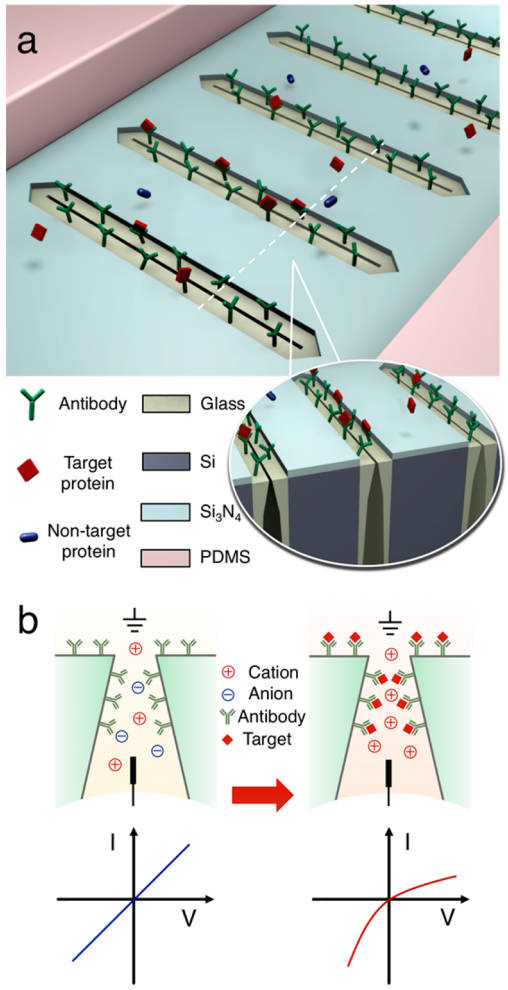

Figure 1. Schematic illustrations of (a) the nanoslit array structure and (b) its biosensing principle. (a) A 3D rendering of the array from above showing selectively functionalized nanoslit regions within a well-defined passivation pattern. Inset: a cutout view revealing the nanoslit array cross-sectional profile. (b) Electrical detection of a target protein based on its intrinsic charge and the consequent modulation of the ionic current rectification through the nanoslit array illustrated at the level of a single nanoslit. Cross-sectional schematics of an antibody-functionalized triangular nanoslit occupied by cations and anions and exhibiting a linear current−voltage (I−V) plot because of the neutral antibody layer. Following the adsorption of negatively charged targets, cations predominantly occupy the nanoslit and the positive currents are suppressed.

is comparable to that of state-of-the-art nanoscaled field-effect sensors, and the device is highly cost-effective and robust, which could possibly pave the way for its use in the development of ultrasensitive, robust, and low-cost diagnostic systems.

The overall integrated device is described in Figure 2a. The device features a nanoslit array at the junction of multilayer crossed-channel architecture; each channel is situated at a distinct layer and the channels are coupled to one another exclusively through the nanoslit array. The 50 μm wide "sample" channel that is situated on top of the nanoslit array was lithographically molded in a cover plate of polydimethylsiloxane (PDMS), whereas the "recording" channel facing the nanoslit array bottom was micromachined into silicon and monolithically integrated with the nanoslit array through a single photomasking process (Supporting Information, Figure S1). Figure 2b shows an optical micrograph of the nanoslit

dx.doi.org/10.1021/nl5032524 | Nano Lett. 2014, 14, 6983−6990

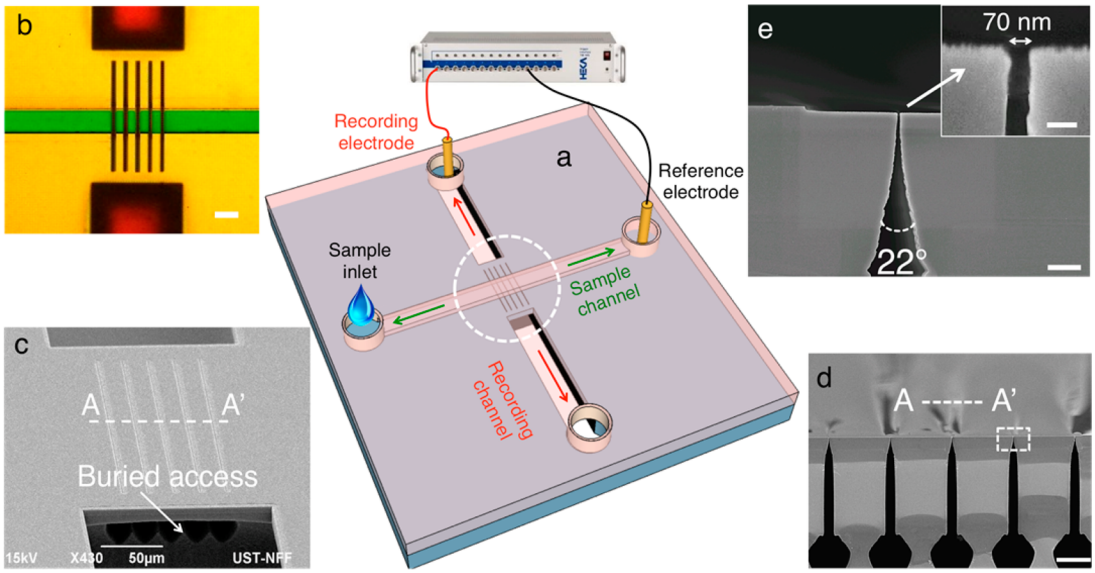

Figure 2. (a) A 3D rendering of the overall integrated biosensor and measurement setup. The dashed circle highlights the nanoslit array at the cross-junction of the sample (green arrows) and recording (red arrows) microfluidic channels, each situated at a distinct layer. (b) Optical micrograph of the nanoslit array captured with the respective channels filled with distinct dye solutions for visualization. (c–e) Scanning electron micrographs depict (c) an oblique view and (d) a cross-sectional (AA′-cut) view of the nanoslit array. The dashed rectangle in (d) highlights a single nanoslit, which is further detailed in (e). Scale bars: (b) 50, (c) 50, (d) 10, and (e) 1 μm (inset: 100 nm).

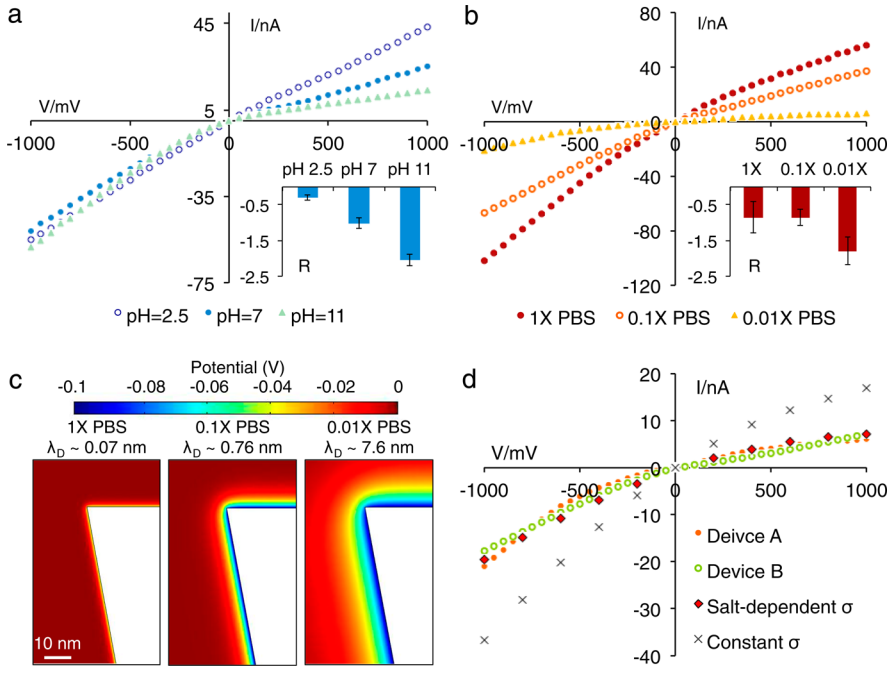

Figure 3. (a,b) Electrical (I–V) characteristics of a representative device measured at distinct (a) pH values (background buffer 10 mM KCl) and (b) ionic strengths (at pH 7.4). Insets: the bar charts indicate the rectification ratio (R) of the respective curves (n = 5). (c) Three 2D simulation plots showing the potential distribution surrounding the nanoslit at various ionic strengths (at pH 7.4) stated above along with the respective screening (Debye) length (λ_D). (d) I–V curves of two representative nanoslit array devices measured using 0.01× phosphate-buffered saline (PBS, pH 7.4) and the respective curves obtained from simulations performed by treating the surface-charge density either as a constant at a typical value of σ = 60 mC/m^2 or as a pH- and salt-dependent variable at σ = 14.6 mC/m^2 evaluated by taking into consideration the influence of the buffer pH and ionic strength on the glass surface.

array featuring the sample and recording channels filled with dye solutions for illustration purposes. A scanning electron micrograph reveals the nanoslit array structure and the recording channel underneath in Figure 2c. The array contains a parallel arrangement of 5 nanoslits that are 200 μm long and are coupled to the channel underneath through buried accesses that are conveniently formed using a characteristic etch profile, which is further exposed in Figure 2d. Each slit tapers upward at an angle of ∼22° and to a surface gap that is ∼70 nm wide (Figure 2e, inset). This unique nanostructure was self-formed because of the use of a nonconformal deposition profile of a glass layer that caused 3 μm wide trench openings to pinch off,

dx.doi.org/10.1021/nl5032524 | Nano Lett. 2014, 14, 6983–6990

thus trapping voids exhibiting a triangular upper segment within these trenches (Supporting Information, Figure S2). The glass layer was then carefully polished in order to flatten the top surface while exposing the nanoscale slits, which made it possible to readily and selectively passivate the surface of the integrated device; a silicon nitride passivation layer was deposited and then removed precisely from around the nanoslits by using the same photomasking and subsequent dry-etching steps.

Because the device features a unique rectifying structure, the asymmetric glass nanoslit, its ionic-rectification behavior was evaluated. Figure 3a shows a representative device's $I-V$ curves that were recorded under symmetric electrolyte conditions at three distinct pH values. The measurement setup is described in Figure 2a and further detailed in Supporting Information. The native glass surface has an isoelectric point (pI) of ~2. Thus, in alkaline (pH 11) and neutral (pH 7) buffers in which the glass surface has an excess negative charge the device exhibits a reasonable rectification, whereas it shows almost no rectification under an acidic condition (pH 2.5) in which the surface charge is strongly quenched. To quantify the extent of ionic current rectification, we defined the logarithmic ratio $R = \log_2(I_{+1v}/I_{-1v})$, where I_{+1v} and I_{-1v} represent the positive and negative current levels at a fixed bias voltage of +1 and −1 V, respectively. This definition aligns with the ratio of rectification previously expressed for nanofluidic diodes.[21,34] The R values calculated for the devices were −0.30, −1.02, and −2.04 at pH 2.5, 7, and 11, respectively (Figure 3a, inset).

We determined that the rectification behavior also depended on the buffer ionic strength (Figure 3b). The plot of the R values in the inset clearly shows that rectification levels increased when buffer concentrations were lowered. The dependence of rectification on ionic strength, as discussed previously,[17] is related to the dominance of the electrical double layer (EDL) within the confined nanochannel/nanopore space. To visualize the EDL, we performed numerical simulations in order to obtain the electric potential distribution surrounding the nanoslit. The simulations were based on a system of Poisson−Nernst−Planck (PNP) equations solved under steady-state conditions as proven effective in quantitatively describing ionic current rectification in conical nanopores.[35] This continuum-based model in its present form, however, has a limited validity in those cases where time-varying processes prevail as in, for instance, ions interacting with the permanent surface charge of the pore or slit walls in a time-dependent manner.[36] These processes, although they were neglected here because of the large slit size and simple electrolyte composition (predominantly NaCl), could be of significance for small pores and electrolytes containing chemically reactive species; the condition of stationary fluxes through such pores or slits no longer holds.[37,38]

Unlike previous reports assuming a constant surface charge density on the pore walls,[35] we considered here a variable surface charge density taking into account the fact that the charge on a silica-based surface in aqueous phase is not constant but rather depends on the bulk ionic strength and pH. This arises from the chemical reactivity of the slit surface, which involves the dissociation of silanol groups ($SiOH \leftrightarrows SiO^- + H^+$); the equilibrium is mainly driven by the local concentration of H^+ ions and local electrostatic potential.[39] We therefore calculated the surface charge by using a surface-reactivity model after Behrens and Grier (Supporting Information, Figure S3, Table S1).[40] In the model, the ions dissociated from the background electrolyte as well as those from the surface were considered, including H^+ ions that potentially accumulate near the slit walls and drive the local pH away from that in bulk solution.[41] Previously, this model has been shown to describe ionic conductance through a single silica nanopore[39] and a submicrometer glass capillary array,[42] which cannot be explained by simply assuming a fixed surface charge. However, when evaluating the ionic currents through the nanoslits, we only considered the fluxes of salt ions (Na^+ and Cl^-) simply because the fluxes of H^+ and OH^- ions simulated under the stated conditions were found negligible.

Figure 3c plots the simulated potential distribution in the nanoslit for the 3 ionic strengths tested. The cold colors at the slit walls indicate negatively charged surfaces at the stated pH 7.4. In 1× phosphate-buffered saline (PBS), the potential decays sharply away from the surface, suggesting the presence of an extremely thin EDL that is negligible in comparison to the nanoslit scale. When the ionic strength is lowered to 0.1× PBS, the EDL is extended, and it is further extended in 0.01× PBS such that it occupies a greater portion of the nanoslit space. The dominance of the EDL in the asymmetric nanoslit is responsible for the ionic current rectification; thus, among the three ionic strengths here, the one that has a thicker EDL would exhibit a greater degree of rectification (Figure 3b). The ionic currents were simulated using both the pH- and salt-dependent surface-charge model and a constant surface charge, and the simulation results were compared with the experimental data measured using two representative devices under the same electrolyte condition (0.01× PBS). The experimental results deviated noticeably from the simulated currents when a constant surface charge was used, whereas the simulated values obtained using a pH- and salt-dependent surface charge agreed very closely with the measurements in terms of both the degree and the polarity of rectifications (Figure 3d). These results empirically and theoretically verify that the 1D confinement of the nanoslit array diodes can support ionic current rectification at acceptable levels.

The fabricated devices were functionalized with anti-cTnT antibodies to selectively target cTnT molecules. As schematically depicted in Figure 4a, the anti-cTnT antibodies were covalently immobilized on the glass surfaces by using silane chemistry.[43] The detailed protocol is presented in Supporting Information. We visualized the functionalization by using FITC-labeled anti-cTnT antibodies. The fluorescence micrograph in Figure 4a clearly shows that the antibodies were selectively anchored around the nanoslits. The progress of the protocol was also monitored based on the $I-V$ characteristics of the devices measured after each step. The recordings were all performed using the same electrolyte, 0.01× PBS (pH 7.4). As shown in Figure 4b, the bare glass surface (pI ~ 2) exhibited a satisfactory rectification level ($R < 0$), whereas the subsequent binding of 3-aminopropyltriethoxysilane (APTES) reversed the rectification polarity ($R > 0$) because of the positively charged amine groups. This implies that not only does the APTES layer shield the intrinsic negative charge of the underlying glass surface, but also leaves a net surface charge that is positive. The linker molecule glutaraldehyde does not carry any charged groups, as a result of which the rectification is nearly lost after the molecules are anchored. The rectification slightly recurs ($R < 0$) upon anti-cTnT binding, which is consistent with a weak negative charge being present on anti-cTnT (pI ~ 7) under the stated buffer condition.[44] After functionalization, the ionic current-rectifying behavior of the nanoslit sensor was also

dx.doi.org/10.1021/nl5032524 | Nano Lett. 2014, 14, 6983−6990

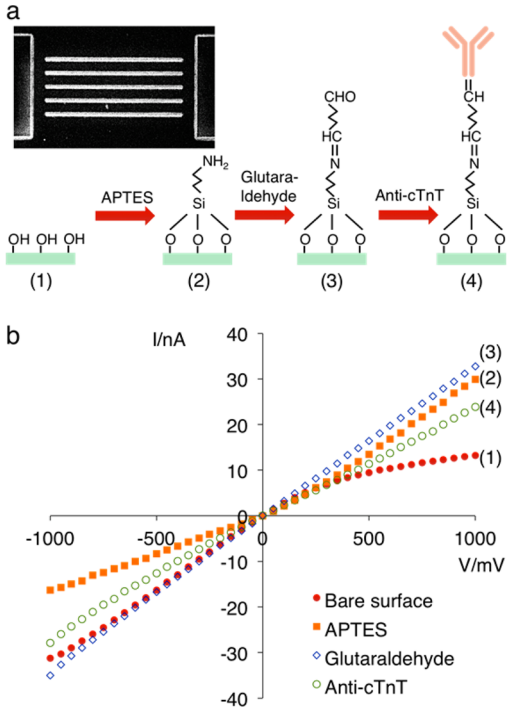

Figure 4. (a) Schematic description of the surface-functionalization protocol and a fluorescence micrograph (top view) of a nanoslit array functionalized with FITC-labeled antihuman cardiac troponin T (anti-cTnT) antibodies. (b) A set of $I-V$ curves obtained from a representative device at specific stages of the functionalization protocol (legend).

characterized under various buffer pH and ionic strength conditions (Supporting Information, Figure S4).

Selectivity is a crucial characteristic that a biosensor must exhibit for use in practical applications. We investigated the selectivity of the nanoslit array sensor by conducting a series of competitive control experiments. In the experiments, the background electrolyte condition used was 0.01× PBS, under which condition the device was confirmed to exhibit optimal rectification. An excessive lowering of the salt concentration was avoided in order to ensure that the proteins retained their biological activity. Figure 5a plots the real-time change of the ratio R measured for an unfunctionalized device that was subjected to consecutive cycles of alternating cTnT injection and wash. The device was subjected to the surface-modification process (Figure 4a) but the anti-cTnT binding step was excluded. The immediate change in R induced by 1 ng/mL cTnT did not persist upon washing and this result was reproducible. These transient signals can be attributed to the cTnT molecules being nonspecifically adsorbed on the surfaces. A similar behavior was also observed in an anti-cTnT-functionalized device when a control protein, tropomyosin, was injected at a concentration of 100 ng/mL (Figure 5b). By contrast, when an anti-cTnT-functionalized device was used for detecting cTnT, permanent responses were measured and the magnitude of the signals (i.e., the change of R) depended on the concentration of the target protein (Figure 5c). These results demonstrate that cTnT was specifically recognized by the anti-cTnT-modified device but not by the one that lacks the specific receptors.

To further evaluate the nanoslit array biosensor and its capacity to resolve various doses of cTnT in a given buffer solution, cTnT (pI ∼ 5.0) was serially diluted to various concentrations in 0.01× PBS, and each dilution was individually assayed using an anti-cTnT-functionalized device. Figure 5d presents the real-time response curves of the sensors measured following the injection of cTnT; the cTnT concentrations varied from 10 fg/mL to 1 ng/mL. The baseline rectification ratio was subtracted to obtain the absolute change $\Delta R = R_D - R_0$, where R_D and R_0 represent the ratio R detected during the experiment and the ratio R recorded immediately after the functionalization, respectively. The results show that when cTnT concentrations were increased, the rectification was gradually lifted to greater negative levels and persisted after the rinse. To improve the visualization of this trend, we derived a calibration curve, which is plotted in Figure 5e. A limit of detection of 10 fg/mL (∼0.3 fM) was routinely achieved at a signal-to-noise ratio that was >3. The calibration curve was linear over 2 orders of magnitude, from 1 to 100 pg/mL, before reaching saturation at 1 ng/mL. These results demonstrate that the nanoslit array sensor can be successfully used for label-free, real-time detection of cTnT down to the femtomole level and over a reasonably large dynamic range. From the fitting of the simulated rectification curves to those experimentally obtained, the surface charge density of the nanoslit array after having been exposed to the stated cTnT concentration range (10 fg/mL to 1 ng/mL) was estimated to be 0.45−2.0 mC/m^2. These values are in reasonable agreement with the estimates reported for the nanopores immobilized with concanavalin A protein (pI 4.5−5.5).[45]

Point-of-care diagnosis requires rapid analysis of complex mixtures, such as blood serum, without further treatment. To test the use of our device for this purpose, we investigated the detection of cTnT in undiluted human serum. We spiked the human serum samples with various concentrations of cTnT antigens. Using the untreated serum samples, which had an ionic strength of ∼160 mM,[46] a signal was barely detected because the EDL was extremely thin. However, we detected a signal after applying a 2 min washing step following incubation with a cTnT-spiked serum sample for 10 min. The experimental procedure used is presented in Supporting Information. Figure 6a shows a set of $I-V$ plots recorded from an anti-cTnT-functionalized device. The trend here shows that when the cTnT dose was increased, the positive currents were gradually suppressed, whereas the negative currents were mostly unchanged. Figure 6b shows the steady-state dose−response relationship. Typical blood-serum samples contain >10 000 protein species with their total content being 7−12 orders of magnitude higher than that of a specific target; therefore, detecting a low-abundance protein can be extremely challenging. The minor shift in R in the case of the untreated serum was possibly caused by nonspecific proteins or by proteins that cross-reacted with anti-cTnT. This background signal appeared to be stable and could not be eliminated using an extended wash cycle (e.g., 30 min). The detection limit was measured to be 10 pg/mL (∼300 fM) cTnT and the average shift in the rectification ratio was ∼0.10 over that of untreated serum. These results demonstrate that the nanoslit array sensor can distinguish cTnT from untreated human serum and exhibit high sensitivity and selectivity in doing so.

As noted in the introductory text, the nanoslit array biosensor and semiconducting nanobiosensors (e.g., nanowires) are similar in that in both the electrostatic field effect is used. However, they differ in the manner in which the field effect is applied. In the case of the nanowire sensors, charges present on the captured biomolecules modulate the surface

dx.doi.org/10.1021/nl5032524 | Nano Lett. 2014, 14, 6983−6990

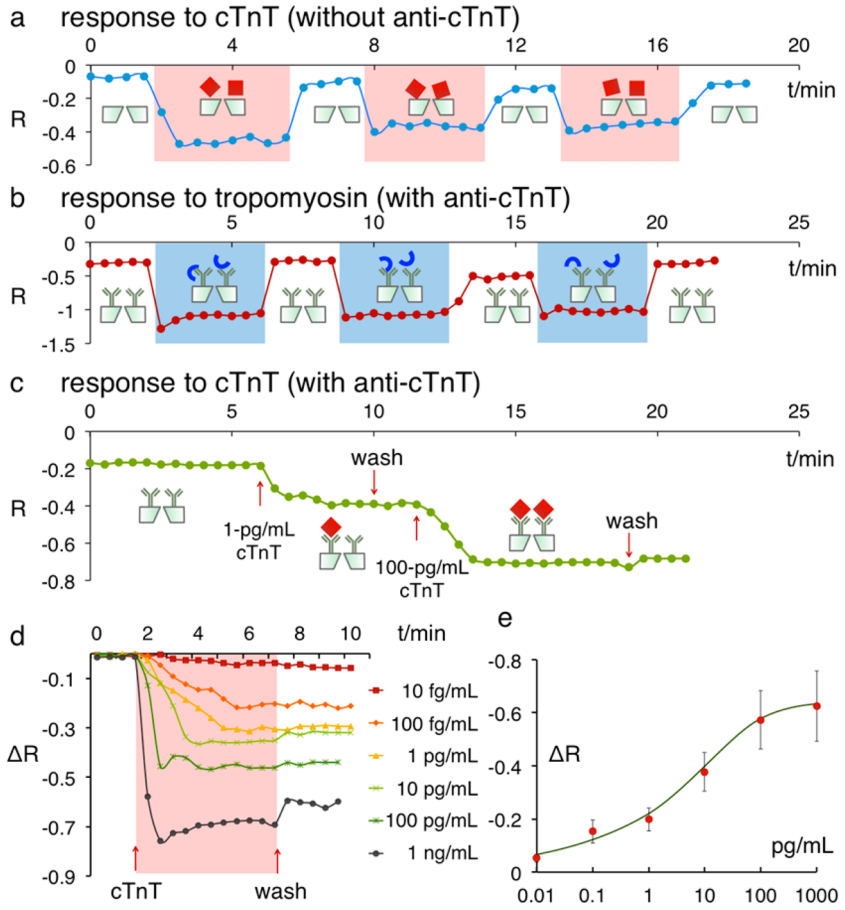

Figure 5. Real-time monitoring of the rectification ratio (R) obtained from (a) a device lacking anti-cTnT during cycles of alternating application of cTnT (1 ng/mL, shaded) and wash; (b) an anti-cTnT-functionalized device during cycles of alternating application of tropomyosin (100 ng/mL, shaded) and wash; and (c) an anti-cTnT-functionalized device during exposure to progressively higher concentrations of cTnT. (d) A set of real-time plots and (e) a calibration curve (n = 5) showing the shift in the rectification ratio (ΔR) at various cTnT concentrations. Each plot in (d) was obtained from a fresh device.

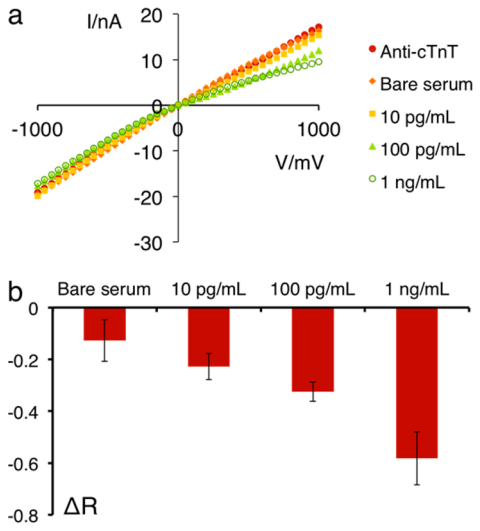

Figure 6. (a) A set of I–V curves measured using a nanoslit array biosensor before (anti-cTnT) and after exposure to human serum spiked with cTnT at various concentrations (legend). (b) Dose–response relationship derived from the measured I–V curves (n = 5) based on the shift in the rectification ratio that is specific to the serum concentration of the cTnT antigen.

potential of the nanowires; this potential change on the surface propagates through the field effect and alters the carrier (electron) concentration within the semiconducting nanomaterial. Therefore, the Debye length can be of a major concern because the EDL formed by counterions can screen off the charges of the molecules.[47] A recent study partly addressed this concern by introducing size-reduced antibody-capturing fragments, with the goal being to reduce the distance between the nanowire surface and the charges on the captured analyte, which can effectively enhance the sensing performance, especially under high ionic strength conditions.[48] However, in the case of the nanoslit array sensor, minimizing the distance between the slit walls and the attached targets is not required because the field effect of the charged molecules directly acts on the electrolyte solution and thereby redistributes the ions and regulates the ionic current rectification. Moreover, because of the immobilized antibodies and the captured targets, the nanoslit space is further confined.

A well-orientated cTnT-antibody bilayer immobilized on the nanoslit surface can potentially reduce the effective gap size from 70 to 20 nm assuming a filamentous protein that is ~16.9 nm long for cTnT (37 kDa),[49] and a globular protein that is ~8 nm in diameter for IgG.[50] This might be favorable because reducing the size of the opening would lead to an enhanced field-effect response. Interestingly, the rectification was found to decrease drastically with an increase in the number of layers of

dx.doi.org/10.1021/nl5032524 | Nano Lett. 2014, 14, 6983–6990

polyelectrolytes on conical nanopores of a small diameter (~20 nm), which was attributed to a nanoconfinement-induced structural reorganization of molecules on conical nanopores.[51] However, this effect was not detected in conical nanopipettes featuring a comparatively larger diameter (~80 nm).[21] Recent studies confirmed such structural reorganization signifying that a typical electrostatic assembly of polyelectrolytes on planar surfaces cannot be simply extrapolated to small nanopores.[52] Surface force studies of polyelectrolyte brushes under confinement showed a significant rearrangement of interacting layers under the repulsion of charge clouds.[53,54] Small-angle neutron scattering analysis of polyelectrolyte chains confined in nanoporous glass suggested a reduced gyration radius and a stretched appearance in relation to the molecules in the bulk.[55] Transmission electron microscopy imaging of polyelectrolyte assemblies in nanoporous templates revealed intermixing of the chains to the extent that a dense gel gets formed.[56,57] It is likely that such structural reorganizations in small nanopores follow from charge regulation with the arrival of polyelectrolyte chains due to their counterion clouds.[52] As the chains being assembled undergo reorganization, surface charge overcompensation vanishes, diminishing the ionic current rectification. However, the structural organization of antibody–antigen pairs in an extremely confined environment and how this will affect the rectification behavior of nanofluidic diodes have yet to be explored.

In conclusion, we have developed a novel nanofluidic diode biosensor featuring an integrated, asymmetric, glass nanoslit array and have demonstrated its utility for sensitive and selective detection of a human cardiac-injury biomarker, troponin T, in PBS as well as in human serum. The results showed that the new integrated nanobiosensor exhibits a sensitivity level that is about >3 orders of magnitude higher than those associated with discrete nanofluidic diodes (e.g., glass nanopipettes, track-etched conical nanopores).[24−28] The shown monolithic integration does not involve high-resolution advanced lithography techniques and can be further scaled up for use in multiplexed assays for the detection of a panel of biomarkers through an inexpensive electronic readout. We are investigating also how the preconcentration and detection steps can be combined into the integrated nanoslit array biosensor.

■ ASSOCIATED CONTENT

Supporting Information

Additional materials related to the fabrication process, experimental methods, and numerical simulation as well as supporting figures. This material is available free of charge via the Internet at http://pubs.acs.org.

■ AUTHOR INFORMATION

Corresponding Author

*E-mail: eelyobas@ust.hk. Phone: +852-2358 7068. Fax: +852-2358 1485.

Notes

The authors declare no competing financial interest.

■ ACKNOWLEDGMENTS

This work was financially supported by the Research Grant Council of Hong Kong under Grant 623912.

■ REFERENCES

(1) Ward, A. M.; Catto, J. W. F.; Hamdy, F. C. *Ann. Clin. Biochem.* **2001**, *38*, 633−651.
(2) Wu, G. H.; Datar, R. H.; Hansen, K. M.; Thundat, T.; Cote, R. J.; Majumdar, A. *Nat. Biotechnol.* **2001**, *19*, 856−860.
(3) Chou, S. F.; Hsu, W. L.; Hwang, J. M.; Chen, C. Y. *Biosens. Bioelectron.* **2004**, *19*, 999−1005.
(4) Cui, Y.; Wei, Q. Q.; Park, H. K.; Lieber, C. M. *Science* **2001**, *293*, 1289−1292.
(5) Patolsky, F.; Zheng, G. F.; Hayden, O.; Lakadamyali, M.; Zhuang, X. W.; Lieber, C. M. *Proc. Natl. Acad. Sci. U.S.A.* **2004**, *101*, 14017−14022.
(6) Stern, E.; Klemic, J. F.; Routenberg, D. A.; Wyrembak, P. N.; Turner-Evans, D. B.; Hamilton, A. D.; LaVan, D. A.; Fahmy, T. M.; Reed, M. A. *Nature* **2007**, *445*, 519−522.
(7) McAlpine, M. C.; Agnew, H. D.; Rohde, R. D.; Blanco, M.; Ahmad, H.; Stuparu, A. D.; Goddard, W. A.; Heath, J. R. *J. Am. Chem. Soc.* **2008**, *130*, 9583−9589.
(8) Lin, Y. H.; Lu, F.; Tu, Y.; Ren, Z. F. *Nano Lett.* **2004**, *4*, 191−195.
(9) Yemini, M.; Reches, M.; Rishpon, J.; Gazit, E. *Nano Lett.* **2005**, *5*, 183−186.
(10) Allen, B. L.; Kichambare, P. D.; Star, A. *Adv. Mater.* **2007**, *19*, 1439−1451.
(11) Chen, R. J.; Bangsaruntip, S.; Drouvalakis, K. A.; Kam, N. W. S.; Shim, M.; Li, Y. M.; Kim, W.; Utz, P. J.; Dai, H. J. *Proc. Natl. Acad. Sci. U.S.A.* **2003**, *100*, 4984−4989.
(12) Cheng, Y.; Chen, K. S.; Meyer, N. L.; Yuan, J.; Hirst, L. S.; Chase, P. B.; Xiong, P. *Biosens. Bioelectron.* **2011**, *26*, 4538−4544.
(13) Zhang, G. J.; Zhang, G.; Chua, J. H.; Chee, R. E.; Wong, E. H.; Agarwal, A.; Buddharaju, K. D.; Singh, N.; Gao, Z. Q.; Balasubramanian, N. *Nano Lett.* **2008**, *8*, 1066−1070.
(14) Zheng, G. F.; Patolsky, F.; Cui, Y.; Wang, W. U.; Lieber, C. M. *Nat. Biotechnol.* **2005**, *23*, 1294−1301.
(15) Hakim, M. M. A.; Lombardini, M.; Sun, K.; Giustiniano, F.; Roach, P. L.; Davies, D. E.; Howarth, P. H.; de Planque, M. R. R.; Morgan, H.; Ashburn, P. *Nano Lett.* **2012**, *12*, 1868−1872.
(16) Eijkel, J. C. T.; van den Berg, A. *Microfluid. Nanofluid.* **2005**, *1*, 249−267.
(17) Cheng, L. J.; Guo, L. J. *Chem. Soc. Rev.* **2010**, *39*, 923−938.
(18) Ali, M.; Mafe, S.; Ramirez, P.; Neumann, R.; Ensinger, W. *Langmuir* **2009**, *25*, 11993−11997.
(19) Nam, S. W.; Rooks, M. J.; Kim, K. B.; Rossnagel, S. M. *Nano Lett.* **2009**, *9*, 2044−2048.
(20) Karnik, R.; Fan, R.; Yue, M.; Li, D. Y.; Yang, P. D.; Majumdar, A. *Nano Lett.* **2005**, *5*, 943−948.
(21) Liu, Y. F.; Yobas, L. *Biosens. Bioelectron.* **2013**, *50*, 78−83.
(22) Yan, R. X.; Liang, W. J.; Fan, R.; Yang, P. D. *Nano Lett.* **2009**, *9*, 3820−3825.
(23) Cheng, L. J.; Guo, L. J. *Nano Lett.* **2007**, *7*, 3165−3171.
(24) Umehara, S.; Karhanek, M.; Davis, R. W.; Pourmand, N. *Proc. Natl. Acad. Sci. U.S.A.* **2009**, *106*, 4611−4616.
(25) Ali, M.; Yameen, B.; Neumann, R.; Ensinger, W.; Knoll, W.; Azzaroni, O. *J. Am. Chem. Soc.* **2008**, *130*, 16351−16357.
(26) Ali, M.; Neumann, R.; Ensinger, W. *ACS Nano* **2010**, *4*, 7267−7274.
(27) Vlassiouk, I.; Kozel, T. R.; Siwy, Z. S. *J. Am. Chem. Soc.* **2009**, *131*, 8211−8220.
(28) Ali, M.; Schiedt, B.; Neumann, R.; Ensinger, W. *Macromol. Biosci.* **2010**, *10*, 28−32.
(29) Karnik, R.; Duan, C. H.; Castelino, K.; Daiguji, H.; Majumdar, A. *Nano Lett.* **2007**, *7*, 547−551.
(30) Perry, J. M.; Zhou, K. M.; Harms, Z. D.; Jacobson, S. C. *ACS Nano* **2010**, *4*, 3897−3902.
(31) Liu, Y. F.; Yobas, L. *Biomicrofluidics* **2012**, *6*, 046502.
(32) Collinson, P. O.; Stubbs, P. J. *N. Engl. J. Med.* **1992**, *327*, 1760−1761.
(33) Adams, J. E.; Bodor, G. S.; Davilaroman, V. G.; Delmez, J. A.; Apple, F. S.; Ladenson, J. H.; Jaffe, A. S. *Circulation* **1993**, *88*, 101−106.

(34) Umehara, S.; Pourmand, N.; Webb, C. D.; Davis, R. W.; Yasuda, K.; Karhanek, M. *Nano Lett.* **2006**, *6*, 2486−2492.
(35) Kubeil, C.; Bund, A. *J. Phys. Chem. C* **2011**, *115*, 7866−7873.
(36) Constantin, D.; Siwy, Z. S. *Phys. Rev. E* **2007**, *76*, 041202.
(37) Siwy, Z. S.; Powell, M. R.; Petrov, A.; Kalman, E.; Trautmann, C.; Eisenberg, R. S. *Nano Lett.* **2006**, *6*, 1729−1734.
(38) Siwy, Z. S.; Powell, M. R.; Kalman, E.; Astumian, R. D.; Eisenberg, R. S. *Nano Lett.* **2006**, *6*, 473−477.
(39) Smeets, R. M. M.; Keyser, U. F.; Krapf, D.; Wu, M. Y.; Dekker, N. H.; Dekker, C. *Nano Lett.* **2006**, *6*, 89−95.
(40) Behrens, S. H.; Grier, D. G. *J. Chem. Phys.* **2001**, *115*, 6716−6721.
(41) Ramirez, P.; Mafe, S.; Aguilella, V. M.; Alcaraz, A. *Phys. Rev. E* **2003**, *68*, 011910.
(42) Cao, Z.; Yobas, L. *Electrophoresis* **2014**, *35*, 2353−2360.
(43) Zhang, G. J.; Tanii, T.; Kanari, Y.; Ohdomari, I. *J. Nanosci. Nanotechnol.* **2007**, *7*, 410−417.
(44) Buis, B.; Wever, P. C.; Koomen, G. C. M.; vanAcker, B. A. C.; Groothoff, J. W.; Krediet, R. T.; Arisz, L. *Nephron* **1997**, *75*, 444−450.
(45) Ali, M.; Ramirez, P.; Tahir, M. N.; Mafe, S.; Siwy, Z.; Neumann, R.; Tremel, W.; Ensinger, W. *Nanoscale* **2011**, *3*, 1894−1903.
(46) Fitzsimons, E. J.; Sendroy, J. *J. Biol. Chem.* **1961**, *236*, 1595−1601.
(47) Stern, E.; Wagner, R.; Sigworth, F. J.; Breaker, R.; Fahmy, T. M.; Reed, M. A. *Nano Lett.* **2007**, *7*, 3405−3409.
(48) Elnathan, R.; Kwiat, M.; Pevzner, A.; Engel, Y.; Burstein, L.; Khatchtourints, A.; Lichtenstein, A.; Kantaev, R.; Patolsky, F. *Nano Lett.* **2012**, *12*, 5245−5254.
(49) Ohtsuki, I.; Onoyama, Y.; Shiraishi, F. *J. Biochem.* **1988**, *103*, 913−919.
(50) Amiry-Moghaddam, M.; Ottersen, O. P. *Nat. Neurosci.* **2013**, *16*, 798−804.
(51) Ali, M.; pt, B.; Cervera, J.; Ramirez, P.; Neumann, R.; Ensinger, W.; Knoll, W.; Azzaroni, O. *J. Am. Chem. Soc.* **2010**, *132*, 8338−8348.
(52) Azzaroni, O.; Lau, K. H. A. *Soft Matter* **2011**, *7*, 8709−8724.
(53) Qu, D.; Pedersen, J. S.; Garnier, S.; Laschewsky, A.; Mohwald, H.; von Klitzing, R. *Macromolecules* **2006**, *39*, 7364−7371.
(54) Zhulina, E. B.; Borisov, O. V. *J. Chem. Phys.* **1997**, *107*, 5952−5967.
(55) Gilbert, E. P.; Auvray, L.; Lal, J. *Macromolecules* **2001**, *34*, 4942−4948.
(56) Alem, H.; Blondeau, F.; Glinel, K.; Demoustier-Champagne, S.; Jonas, A. M. *Macromolecules* **2007**, *40*, 3366−3372.
(57) Roy, C. J.; Dupont-Gillain, C.; Demoustier-Champagne, S.; Jonas, A. M.; Landoulsi, J. *Langmuir* **2010**, *26*, 3350−3355.